The Astrophysical Journal, 982:76 (12pp), 2025 April 1 https://doi.org/10.3847/1538-4357/adb48b

Turbulent Suppression of Alfvénic Wave Resonances in Coronal Loops

Edris Tajfirouze[1], Richard Morton[1], and Mahboubeh Asgari-Targhi[2]
[1] Department of Mathematics, Physics and Electrical Engineering, Northumbria University, Newcastle upon Tyne, UK; edris.tajfirouze@northumbria.ac.uk
[2] Harvard Smithsonian Center for Astrophysics, 60 Garden Street, Cambridge, MA 02138, USA
Received 2024 November 19; revised 2025 February 10; accepted 2025 February 10; published 2025 March 20

Abstract

Alfvénic wave turbulence is a leading mechanism for explaining the heating of the solar corona and the acceleration of the solar wind. Alfvénic waves are observed to be prevalent throughout the inner corona. An intriguing aspect of the observed waves is that active-region loops show decayless standing Alfvénic oscillations, while quiet-Sun loops show only propagating Alfvénic waves. Given the weaker rates of resonant damping found in the quiet Sun (compared to those estimated from decaying oscillations of active-region loops), the reason for the lack of observed standing oscillations is unclear. We suggest that this may be due to the presence of efficient (or strong) Alfvénic wave turbulence in the quiet Sun, which limits the ability of waves to form resonant oscillations in the coronal cavity. To test this idea, we model the coronal velocity fluctuations using a previously developed 3D reduced magnetohydrodynamic model. In this model, we implement a semi-realistic profile for atmospheric plasma conditions along the magnetic field and a homogeneous plasma perpendicular to the magnetic field. Results are presented for different models of the background atmosphere that effectively have different levels of coronal turbulence. For the Alfvénic waves in the simulation, we see that resonant modes are present when the coronal turbulence is in a weak regime. However, decreasing the nonlinear timescale leads to a faster development of turbulence. This can suppress the presence of standing modes when the nonlinear timescale is comparable to or shorter than the Alfvén travel time.

Unified Astronomy Thesaurus concepts: Solar coronal heating (1989); Solar coronal waves (1995); Solar physics (1476); The Sun (1693); Quiet solar corona (1992); Active solar corona (1988); Magnetohydrodynamics (1964)

1. Introduction

The Sun's corona is a highly inhomogeneous plasma, with variations both parallel and perpendicular to the magnetic field. The perpendicular inhomogeneity is characterized by overdense flux tubes that highlight the unseen magnetic field (for example, coronal loops, e.g., M. J. Aschwanden et al. 2000). The perpendicular inhomogeneity occurs on short scales (100–1000 km) perpendicular to the magnetic field (e.g., P. Antolin & L. Rouppe van der Voort 2012; D. H. Brooks et al. 2013; R. J. Morton & R. Cunningham 2023), in comparison to the large pressure and magnetic scale heights (10^4–10^5 km). There is a question as to whether the corona is composed of discrete overdense flux tubes or more extended and diffuse objects (A. Malanushenko et al. 2022). Regardless of the underlying structure, the corona is known to be replete with Alfvénic waves (S. Tomczyk et al. 2007; R. J. Morton et al. 2015). We use the term "Alfvénic" as it describes magnetohydrodynamic waves in inhomogeneous plasma that have properties reminiscent of the pure Alfvén waves. They are transverse oscillations that are highly incompressible and have magnetic tension as the restoring force (M. Goossens et al. 2009, 2012).

Alfvénic waves are a generalization of a surface Alfvén wave that occurs at a simple plasma interface (D. G. Wentzel 1979; B. Roberts 1981). Hence the term Alfvénic is likely an applicable descriptor for the highly incompressible waves observed to propagate in the complex structured coronal plasma. These transverse motions are often considered as promising candidates to heat the solar corona as well as accelerating the solar wind (S. W. McIntosh et al. 2011; I. Arregui 2015; T. Van Doorsselaere et al. 2020). At present, a possible mechanism for effective dissipation of the Alfvénic waves is MHD turbulence (e.g., J. V. Hollweg 1983; F. Rappazzo et al. 2007; A. A. van Ballegooijen et al. 2011; A. Verdini et al. 2012). In this scenario, propagating waves reflect due to plasma inhomogeneity along the magnetic waveguide. This results in a system of counterpropagating waves that can interact nonlinearly, allowing for the energy to cascade from large scales to small scales, where the dissipation processes are more efficient. Additionally, recent work suggests that reflection may not always be the key, as surface Alfvénic waves can undergo a self-interaction to invoke a turbulent cascade (N. Magyar et al. 2017, 2019).

1.1. Observations of Coronal Loop Oscillations

Current observations suggest that there appear to be two populations of Alfvénic modes in the corona: standing modes that are present in the active regions (e.g., S. A. Anfinogentov et al. 2015) and propagating waves in the quiet Sun (e.g., R. J. Morton et al. 2016).

Standing modes were identified in the 1990s with the launch of the Transition Region and Coronal Explorer. Active-region coronal loops were seen to undergo standing-mode oscillations, excited by nearby magnetic reconnection events (M. J. Aschwanden et al. 1999; V. M. Nakariakov et al. 1999). In the literature, these waves were referred to as the kink mode (T. Van Doorsselaere et al. 2008) because the loops demonstrate a periodic transverse displacement of the loop axis (the fundamental radial modes of non-axisymmetric oscillations, e.g., kinks, are manifestations of surface Alfvén modes; see M. Goossens et al. 2012). The standing

modes are rapidly damped, typically within a few periods. Since the initial observations, hundreds of standing modes have been observed (C. R. Goddard et al. 2016), with the rapid damping attributed to resonant absorption, a process that relies on the presence of a density inhomogeneity and converts the swaying motion to a rotational Alfvénic mode (J. A. Ionson 1978; M. S. Ruderman & B. Roberts 2002; J. Terradas et al. 2008; M. Goossens et al. 2011). Usually the observations are of the fundamental modes of the system, but there have also been identifications of the second and third harmonics (e.g., E. Verwichte et al. 2004; T. J. Duckenfield et al. 2019). The strength of the observed wave damping can be given by the quality factor.[3] Observational estimates reveal that there is a distribution of quality factor values, which has a median of ∼1.8 for the decaying standing modes (e.g., R. J. Morton et al. 2021).

These impulsively driven standing modes are relatively infrequent and are not the standing modes of interest here. More recently there has been the identification of the so-called *decayless* standing modes, which appear to be common but are found only within active regions (T. Wang et al. 2012; G. Nisticò et al. 2013; S. A. Anfinogentov et al. 2015; S. Mandal et al. 2021). These waves also appear to be the standing kink mode, with a coronal velocity amplitude of the order of 1–4 $\mathrm{km\,s^{-1}}$ (S. W. McIntosh et al. 2011; H. Tian et al. 2012; V. M. Nakariakov et al. 2016). However, they do not show the rapid decay associated with impulsively driven standing modes. They are apparently driven continuously and present for many oscillatory cycles. The source of the driving is assumed to be random footpoint motions. A case has been made that the system is well described as a small-amplitude Rayleigh oscillator, where the damping balances the driving and keeps the system relatively stable (V. M. Nakariakov et al. 2016; A. N. Afanasyev et al. 2020; K. Karampelas & T. Van Doorsselaere 2020; V. M. Nakariakov & D. Y. Kolotkov 2020).

We also note that these decayless waves are not necessarily the only type of Alfvénic oscillations present in active regions. Measurements of coronal line widths in active regions provide varying estimates for nonthermal velocities, with a range of 15−37 $\mathrm{km\,s^{-1}}$ (e.g., M. Asgari-Targhi et al. 2014, 2024; D. H. Brooks & H. P. Warren 2016). The nonthermal velocities can be associated with unresolved Alfvénic wave motions.

The other population of Alfvénic waves are the propagating kink modes in the quiet Sun, first identified by S. Tomczyk et al. (2007) with the Coronal Multi-Channel Polarimeter (CoMP). The results from CoMP do not indicate that standing modes are present in the quiet Sun, only propagating waves. The propagating waves are known to be present throughout the quiescent corona and over the solar cycle (R. J. Morton et al. 2019). In contrast to the active-region wave modes, the propagating waves only appear to be weakly damped by resonant processes as they propagate (R. J. Morton et al. 2021; A. K. Tiwari et al. 2021), around a factor of 10 less (median quality factor of 11) than the rapid damping observed with the impulsively driven standing modes.

1.2. The Puzzle

The presence of the two distinct populations of Alfvénic waves that arise in the quiet Sun and in the active regions raises the questions: Why should this be the case? Why are there no standing modes in the quiet Sun? The presence of standing modes is perhaps the most straightforward to comprehend. From linear theory, it is expected that energy injection into the closed magnetic structures, such as coronal loops, leads to resonant (standing) modes being excited within the coronal cavity (J. A. Ionson 1982; J. V. Hollweg 1984). The resonant modes of the cavity occur at frequencies given by

$$f = \frac{nV_{\mathrm{AC}}}{2L_C}, \tag{1}$$

where V_{AC} is the coronal Alfvén speed, L_C is the length of the coronal segment, and $n = 1, 2, \ldots$ is the order of the harmonic mode. The transition region provides a permeable barrier for waves coming from below and those trapped in the cavity, with the degree of permeability dependent upon frequency. This leads to a leakage of wave energy from the corona, which can reduce the buildup of energy in the cavity and decreases the dissipation (compared to a line-tied system). However, the leakage time is generally considered to be much greater than the Alfvén crossing time $t_{\mathrm{A}} = L_C/V_{\mathrm{A}_C}$ (L. Ofman 2002).

For footpoint-driven oscillations, the excitation of standing modes occurs regardless of the shape of the driving spectrum (A. N. Afanasyev et al. 2020; V. M. Nakariakov et al. 2022), although there will likely be a dependence between the shape of the driving spectrum at the footpoints and the number of resonant frequencies present in observed oscillating coronal loops. For example, for linear waves excited in the system, the driver will have to contain significant power at high frequencies in order to excite high-frequency harmonics within the resonant cavity. For the decayless standing modes, the energy input is potentially balanced by wave damping (resonant or other). This stops the wave amplitude growing in response to the continuous forcing. In contrast, the impulsively driven standing modes decay rapidly as the energy input is transient and due to an eruptive event (I. V. Zimovets & V. M. Nakariakov 2015).

However, the propagating waves are continually present in the quiescent corona, suggesting they are also near-continually excited (e.g., R. J. Morton et al. 2016, 2019). It should then be expected that the quiescent coronal loops would also show signatures of standing modes, even more so given that the resonant damping appears much weaker than in active regions (R. J. Morton et al. 2021). Yet there is no evidence for standing modes in the CoMP data.[4]

Inspired by these observational cases, we are interested in whether wave turbulence could provide an explanation for such phenomena. More specifically, whether the existence of only propagating waves in closed field geometries may be a result of how the wave turbulence develops. In Section 2 we present a phenomenological argument for why resonant modes may not be seen in the quiescent Sun. We back this up with numerical simulations of Alfvénic wave turbulence in a closed magnetic field shown in Sections 3 and 4. In Section 4 we discuss how the results of these simulations may transfer to the observed case of the kink mode (which requires the presence of magnetic or density inhomogeneity perpendicular to the magnetic field direction).

[3] For standing modes this is the ratio of the period to the damping timescale.

[4] This fact has been successfully exploited to map the coronal magnetic field through coronal seismology, where the propagation speed of the waves is estimated and inverted (Z. Yang et al. 2020).

2. A Phenomenological Picture

Let us first introduce two important timescales that are necessary for understanding the development of wave turbulence. The presence of a magnetic field imposes anisotropy on the spectrum of turbulent systems and is the basis of the P. Goldreich & S. Sridhar (1995) description of the dynamics of turbulence. The first timescale is that of the wave dynamics,

$$\tau_{\rm A} \sim \frac{l_\parallel}{v_{\rm A}}, \tag{2}$$

and is associated with wave scales parallel to the mean magnetic field ($l_\parallel \sim k_\parallel^{-1}$). $\tau_{\rm A}$ is the Alfvén travel time if $l_\parallel$ is equal to the loop length. The Alfvén travel time is the upper limit for this timescale, as $l_\parallel$ cannot be longer than the length of the loop. The second timescale is associated with nonlinear effects,

$$\tau_{\rm nl} \sim \frac{\lambda}{\delta u_\lambda}, \tag{3}$$

where δu_λ is the size of the velocity fluctuations at scale λ. This describes the perpendicular variations on scales $\lambda \sim k_\perp^{-1}$ associated with nonlinear interactions due to turbulence. This timescale is viewed as the time taken for a wave packet of size λ to decorrelate (or break up) due to nonlinear interactions. In a fully developed Alfvénic turbulence the fluctuations are expected to reach a critical balance in which the nonlinear time is comparable to the Alfvén travel time (P. Goldreich & S. Sridhar 1995; S. Oughton & W. H. Matthaeus 2020). The ratio of these two terms provides a measure of the nonlinear to linear effects, i.e.,

$$\zeta = \frac{\tau_{\rm A}}{\tau_{\rm nl}} \approx \frac{k_\perp \delta u}{k_\parallel v_{\rm A}}. \tag{4}$$

It should be expected that if $\zeta \ll 1$ for some scale λ then the wave dynamics are influential and the development of nonlinear dynamics happens slowly. Hence, fluctuations associated with the scale λ should be able to propagate along the coronal loop without significant distortion due to turbulence. This is often referred to as the weak turbulence regime. It is also expected that there is little or no parallel cascade in this regime, with the transfer of energy primarily in the perpendicular direction (e.g., S. V. Nazarenko & A. A. Schekochihin 2011; R. Meyrand et al. 2016; S. Oughton & W. H. Matthaeus 2020; A. A. Schekochihin 2022).

On the other hand, if $\zeta \sim 1$, then the system is said to be in a strong turbulence regime or critical balance. In this regime the nonlinear effects play a key role and wave packets can be severely distorted even after a single crossing time of oppositely propagating waves (P. Goldreich & S. Sridhar 1995). In such a regime, there is also a parallel cascade although it is suppressed compared to the perpendicular cascade (A. Beresnyak 2015; R. Meyrand et al. 2019). In a system with a strong turbulence, $l_\parallel$ is the distance that an Alfvénic wave will travel along the magnetic field in the time $\tau_{\rm nl}$. As discussed by A. A. Schekochihin (2022), by causality, $l_\parallel$ is determined by the nonlinear timescale because "no structure longer than $l_\parallel \sim v_{\rm A}\tau_{\rm nl}$ can be kept coherent and so will break up" (see also, e.g., S. Boldyrev 2005; S. V. Nazarenko & A. A. Schekochihin 2011).

It is suggested that a system will likely not remain within a weak turbulence regime and will evolve toward a strong turbulence regime (A. A. Schekochihin 2022). There is likely a perpendicular scale at which the nonlinear time is comparable to the Alfvén travel time and there is transition into a strong turbulence regime (the transition from weak to strong regimes has been observed in numerical simulations, see R. Meyrand et al. 2016).

One could then see that, in a continually driven coronal loop system where $\tau_{\rm A} \gtrsim \tau_{\rm nl}$, each wave packet will suffer many nonlinear interactions as it meets many counterpropagating wave packets while traveling along the loop. Hence, energy is transferred to smaller perpendicular and parallel wavenumbers before a wave packet is able to propagate the effective distance required for setting up a standing mode (i.e., two times the loop length). Therefore, for coronal loops in which there is strong wave turbulence at the scales (i.e., wavenumbers) associated with the resonances, resonant modes may not be able to form as the nonlinear dynamics dominate the wave dynamics. In contrast, if $\tau_{\rm A} \ll \tau_{\rm nl}$ then the linear wave dynamics will dominate and resonant modes can be set up before a turbulent state has developed. While slightly different in scope, P. Dmitruk & W. H. Matthaeus (2003) also show the importance of the ordering of key timescales on the efficiency of imbalanced turbulence and its development. In particular, they report that efficient wave dissipation can occur if the nonlinear timescale is proportional to or less than the Alfvén crossing time.

It is then of interest to consider the situation with respect to the Alfvénic waves in the corona. For standing modes the parallel scale, $l_\parallel$, can be associated with the length of the coronal loops. There are no measurements yet for the parallel scales associated with observed propagating Alfvénic waves. For now, we will also assume the loop length is the length scale associated with the propagating mode. From previous wave studies, average loop lengths are around 300 Mm (S. A. Anfinogentov et al. 2015; A. Nechaeva et al. 2019; A. K. Tiwari et al. 2021).[5] The typical phase speed of Alfvénic waves in active-region coronal loops is at least of the order of 1000 km s^{-1} (S. A. Anfinogentov & V. M. Nakariakov 2019), while in quiescent-Sun loops the values are around 300–700 km s^{-1} (e.g., Z. Yang et al. 2020; A. K. Tiwari et al. 2021, which is to be expected due to the weaker magnetic fields in the quiescent Sun). This gives typical Alfvén travel times of 300 s in active regions and 750 s in the quiescent Sun.

The largest perpendicular scale, $l_\perp$, for coronal loops could be taken as the loop width. Coronal loops typically have widths of the order of ∼640 km (D. H. Brooks et al. 2013). However, recent work by R. Sharma & R. J. Morton (2023) suggests that Alfvénic motions are spatially coherent perpendicular to the magnetic field on scales of ∼6000 km. This implies that a number of loops oscillate coherently and energy injection can occur on scales larger than individual loops.

Aside from kink motions, the magnitudes of other Alfvénic modes in the solar corona are unknown. Rotational motions have only been reported in specific events (e.g., surges—P. Kohutova et al. 2020). In the chromosphere, the velocity amplitudes of rotational and kink motions appear to be comparable (B. De Pontieu et al. 2012). We see no reason

[5] This value is biased toward loops where the oscillations have been detected. For example, CoMP can only observe loops with lengths greater than 100 Mm. It is known that coronal loops exist with lengths starting from ∼10 Mm (e.g., F. Reale 2014; E. Petrova et al. 2023).

why this should be different in the corona. Hence, we use the observed velocity amplitudes of kink motions as a guide. One could use nonthermal broadening of spectral lines as an indicator of Alfvénic waves, but the nonthermal broadening will contain other unresolved motions along the line of sight. Hence, here we prefer to use the direct measurements of Alfvénic waves as an indicator of mode amplitudes. The velocity fluctuations for the decayless waves have amplitudes of 1–4 km s^{-1} in the corona (S. A. Anfinogentov et al. 2015), while the coronal amplitudes are much larger for propagating waves at 20 km s^{-1} (S. W. McIntosh et al. 2011; R. J. Morton et al. 2019). Depending on the perpendicular scale, the nonlinear timescales estimated using Equation (3) are 3000 s (320 s)[6] in active regions and 300 s (32 s) in the quiescent Sun.

While this is an approximate calculation, it can be seen that the nonlinear time is expected to be shorter than the Alfvén travel time in the quiescent Sun, $\zeta \gtrsim 1$. This implies that for the quiescent-Sun loops the value of $l_{\parallel}$ is not necessarily the loop length due to a strong decorrelation of the wave packets. Hence, $l_{\parallel}$ will likely be shorter if the turbulence is strong such that $\zeta = 1$. In contrast to the quiet Sun, the ratio of wave timescales to nonlinear timescale in active regions is $\zeta \lesssim 1$. We note that this does not rule out the development of turbulence in active-region loops. Even though $\tau_{\rm A} < \tau_{\rm nl}$ the system would still develop into a turbulent state. It is just that this happens more slowly than the timescale associated with the wave propagation.

3. RMHD Model

In this section we discuss the numerical simulations of Alfvénic wave turbulence in a reduced magnetohydrodynamic (RMHD) model. The model that we use here is a three-dimensional magnetohydrodynamic model that simulates the dynamics of Alfvén waves inside a single flux tube. This model was developed by A. A. van Ballegooijen et al. (2011) and the assumptions inherent in it remain applicable (we refer readers to the original paper for a full discussion). A. A. van Ballegooijen et al. (2011) used a realistic model of the background atmosphere in their study. However, in this paper, we changed the initial conditions of the model and introduced a semi-realistic background atmosphere. We briefly summarize aspects of the RMHD model here.

3.1. Governing Equations

The waveguide consists of a thin vertical flux tube that extends from photosphere to the corona. The inclusion of gravity allows for the density and pressure stratification along the loop. The transition region is included but is not well resolved. The two ends of the flux tube are anchored at the photosphere and are not correlated. The neighboring field lines are not merged, therefore no magnetic reconnection occurs and the flux tube retains its identity for the whole run time of the simulation. The tube has a circular cross section with radius R (z) that varies with height to hold the conservation of magnetic flux all through the entire loop length.

[6] The first value is the timescale using the estimated perpendicular scale of coronal waves, while the value in parenthesis is using the loop width to set the perpendicular scale.

The dynamics of the waves along a single flux tube are described using the equation of motion:

$$\rho\frac{d\boldsymbol{v}}{dt} = -\nabla\ p + \rho\boldsymbol{g} + \frac{1}{4\pi}(\nabla\ \times \boldsymbol{B}) \times \boldsymbol{B} + \boldsymbol{D}_{\nu} \tag{5}$$

and the magnetic induction equation:

$$\frac{\partial \boldsymbol{B}}{\partial t} = \nabla\ \times (\boldsymbol{v} \times \boldsymbol{B}) + \boldsymbol{D}_{m} \tag{6}$$

where $\rho(\boldsymbol{r}, t)$ is the plasma density, $p(\boldsymbol{r}, t)$ is the pressure, $\boldsymbol{v}(\boldsymbol{r}, t)$ is the velocity, $\boldsymbol{B}(\boldsymbol{r}, t)$ is the magnetic field, $\boldsymbol{g} = g_0(z)\hat{z}$ is the gravity, with g_0 the effective gravitational acceleration. Note that gravity has no component transverse to the loop. $\boldsymbol{D}_{\nu}$ and $\boldsymbol{D}_{m}$ are viscous and resistive dissipation terms. To simplify the description of the dynamics in the system, the magnetic field and the velocity are considered to be sums over the mean values and the perturbed components:

$$\boldsymbol{B} = \boldsymbol{B}_0 + \boldsymbol{B}_1 + ... \tag{7}$$

$$\boldsymbol{v}_{\perp} = \boldsymbol{v}_{\perp,0} + \boldsymbol{v}_{\perp,1} + ... \tag{8}$$

Parallel velocity, density, and pressure are also considered in the same manner. An RMHD approximation (H. R. Strauss 1976) is used, which assumes that the magnetic fluctuation is much smaller than the background magnetic field. Furthermore, there is the assumption that the transverse length scale $l_{\perp}$ of the waves is less than the tube radius ($l_{\perp} \leqslant R$) and is small compared to the parallel scale ($l_{\parallel}$). Therefore, a key small parameter is

$$\varepsilon \equiv \max\left(\frac{u_{\perp}}{v_{\rm A}}, \frac{l_{\perp}}{l_{\parallel}}\right) \ll 1. \tag{9}$$

So, the magnetic and velocity fields can be expanded in powers of ε:

$$\boldsymbol{B} = \boldsymbol{B}_0 + \boldsymbol{B}_1 + \mathcal{O}(B_{00}\varepsilon^2) \tag{10}$$

$$\boldsymbol{v}_{\perp} = \boldsymbol{v}_{\perp,1} + \boldsymbol{v}_{\perp,2} + \mathcal{O}(v_{\rm A}\varepsilon^3). \tag{11}$$

In addition, the model uses the thin-tube approximation:

$$\varepsilon_0(z) \equiv \frac{R(z)}{H_B(z)} \ll 1 \tag{12}$$

which means that the radius of the tube is much smaller than the magnetic scale height. It assumes the following approximation for the magnetic field:

$$\boldsymbol{B}_0 = B_{00}\hat{z} - \frac{1}{2}\frac{dB_{00}}{dz}(x\hat{x} + y\hat{y}) + \mathcal{O}(B_{00}\varepsilon_0^2) \tag{13}$$

where B_{00} is the field strength on the tube axis ($x = y = 0$). The magnetic field is taken to be divergence-free and the motions are assumed to be incompressible.

The induction equation can be rewritten as

$$\frac{\partial \boldsymbol{A}}{\partial t} = \boldsymbol{v}_{\perp} \times \boldsymbol{B} + \nabla\phi \tag{14}$$

in which $A(\boldsymbol{r}, t)$ is the vector potential and ϕ is the electric potential, and the following description can be considered for the first-order perturbation of the vector potential (H. R. Strauss 1997):

$$\boldsymbol{A}_1(\boldsymbol{r}, t) = \boldsymbol{h}(\boldsymbol{r}, t)\boldsymbol{B}_0(\boldsymbol{r}) \tag{15}$$

where h is the magnetic flux function ($h \sim l_\perp \varepsilon$). Then, the magnetic field and the perpendicular component of velocity $v_\perp$ can be rewritten in terms of magnetic flux function h and stream function ($f \equiv \varphi(\boldsymbol{r}, t)/B_0(\boldsymbol{r})$) respectively.

The twist parameter is defined as

$$\alpha(\boldsymbol{r}, t) \equiv -\nabla_\perp^2 h \tag{16}$$

and the parallel vorticity as

$$\omega \equiv \hat{\boldsymbol{B}}_0 \cdot (\nabla \times \boldsymbol{v})) \approx -\nabla_\perp^2 f. \tag{17}$$

In analogy to the Elsässer variables, we define the following two variables (W. M. Elsasser 1950):

$$\omega_\pm \equiv \omega \pm v_\mathrm{A}\alpha \quad \text{and} \quad f_\pm \equiv f \pm v_\mathrm{A} h. \tag{18}$$

Using these quantities, which are scalars unlike velocity and magnetic field, one can obtain the following equation that describes the dynamics of Alfvén waves using the stream function and magnetic flux function:

$$\frac{\partial \omega_\pm}{\partial t} = \pm v_\mathrm{A}\hat{\boldsymbol{B}}_0 \cdot \nabla \omega_\pm - v_\mathrm{A}\frac{dv_\mathrm{A}}{dz}\alpha - [\omega_\pm, f_\mp] \pm \mathcal{N} \tag{19}$$

where the nonlinear term $\mathcal{N}$ is defined by

$$\mathcal{N} \equiv \left[\frac{\partial f_+}{\partial x}, \frac{\partial f_-}{\partial x}\right] + \left[\frac{\partial f_+}{\partial y}, \frac{\partial f_-}{\partial y}\right] \tag{20}$$

and [..., ...] is the bracket operator, which is defined by

$$[a, b] \equiv \frac{\partial a}{\partial x}\frac{\partial b}{\partial y} - \frac{\partial a}{\partial y}\frac{\partial b}{\partial x}. \tag{21}$$

In the above equation ω_+ and ω_- describe the inward and outward propagating waves respectively ($\mp\hat{\boldsymbol{B}}_0$ directions). The first two terms on the right-hand side describe the linear coupling, and the last two terms describe the nonlinear coupling.

The longitudinal dependence of the wave equation is solved on a uniform spatial grid in terms of Alfvén travel time from the photosphere to the corona using an explicit method. The transition region is considered as a discontinuity and is represented by two grid points at the same position but with different densities. The transition from an Alfvén speed of $<20\,\mathrm{km\,s^{-1}}$ in the chromosphere to a much greater coronal Alfvén speed (at least $380\,\mathrm{km\,s^{-1}}$ in the simulations undertaken here) leads to significant wave reflection (J. V. Hollweg 1981). The propagation of the waves at the transition region is described by reflection and transmission coefficients (see Appendix B of A. A. van Ballegooijen et al. 2011).

3.2. Wave Dynamics

The initial atmosphere is perturbed by two counterrotating cells at the base of the flux tube to mimic small random footpoint motions inside the flux tube at the photosphere. The motions are assumed to be restricted to the cross section of the loop. The model uses a spectral method to simulate the random footpoint motions inside the loop cross section and assumes that functions on a circular area can be decomposed into orthogonal basis function $F_i(\xi, \varphi)$ where ξ is the relative distance from the tube axis ($\xi \equiv r/R$) and index i enumerates the basis function. The basis function is the eigenfunction of the $\nabla_\perp^2$ operator:

$$R^2 \nabla_\perp^2 F_i(\xi, \varphi) = \lambda_i F_i(\xi, \varphi) \tag{22}$$

where λ_i is the dimensionless eigenvalue and $F_i(\xi, \varphi)$ are proportional to the Bessel function $J_m(a_i\xi)$. The parameter m is the azimuthal wavenumber and a_i are the zeros of the Bessel function. The modes are ordered according to their m values, and for a specific m the modes are ordered by their a values. The eigenvalues of the modes are $\lambda_i = -{a_i}^2$. The values of a_k are taken as the dimensionless perpendicular wavenumber.

The footpoint motions can be described by superposition of two modes. In our work we selected two successive modes labeled by $m = 1$, which are orthogonal and are the seventh (proportional to $\sin\varphi$) and eighth (proportional to $\cos\varphi$) eigenmodes of Equation (22). Both modes have the same radial dependence ($a = 3.832$). This pattern can be shown mathematically in terms of a stream function as

$$f(r, \varphi, 0, t) = f_7(t)F_7(r/R_\mathrm{phot}, \varphi) + f_8(t)F_8(r/R_\mathrm{phot}, \varphi) \tag{23}$$

where f_7 and f_8 are the mode amplitudes that are created by a random normal distribution on a grid of time covering the entire run time of the simulation (3000 s). The rms velocity of the combined pattern of the two modes is $\Delta v_\mathrm{rms} = R_\mathrm{phot}\omega_0\sqrt{1/a_7^2 + 1/a_8^2}$ where a_7 and a_8 are the perpendicular wavenumbers of the seventh and eighth modes respectively and the quantity ω_0 is a free parameter of the model that effectively controls the amplitude of the wave driver. The driver modes generate rotational Alfvén waves, which can interact nonlinearly to cascade to higher-order m and a_i.

The waves are excited by a multifrequency driver where the correlation time for the photospheric motions tends to zero. The power spectrum of the driver is spectrally flat and hence is equivalent to white noise. We note that a spectrally flat power spectrum is likely not representative of observed photospheric motions. The horizontal displacement of photospheric magnetic bright points shows a power-law dependence on frequency (L. P. Chitta et al. 2012). The choice of utilizing the nonphysical driver is made because it is more instructive. The chosen driver will excite many harmonics in a closed structure (at least in a linear model) and hence enables clear visualization of resonant structures. Using a realistic driver would likely excite fewer of the resonant frequencies in the loop because the energy flux at high frequencies would potentially be too small to sustain the associated resonance behavior against any dissipation. Hence, one should expect to find less energy in the higher-frequency resonances in the corona than is seen in our results. We have confirmed that the following results also hold when using a more realistic photospheric driver. Additional simulations were undertaken in which the photospheric power spectrum follows a frequency-dependent power law. The main difference is that only the low-frequency resonances were found to be present in the system with small nonlinearity. Hence, we choose to present the following results only, as they highlight the impact on resonant structure with more clarity.

3.3. Simulation Setup

In order to show the impact of varying the characteristic temporal scales (i.e., those of the wave dynamics, τ_A, and the

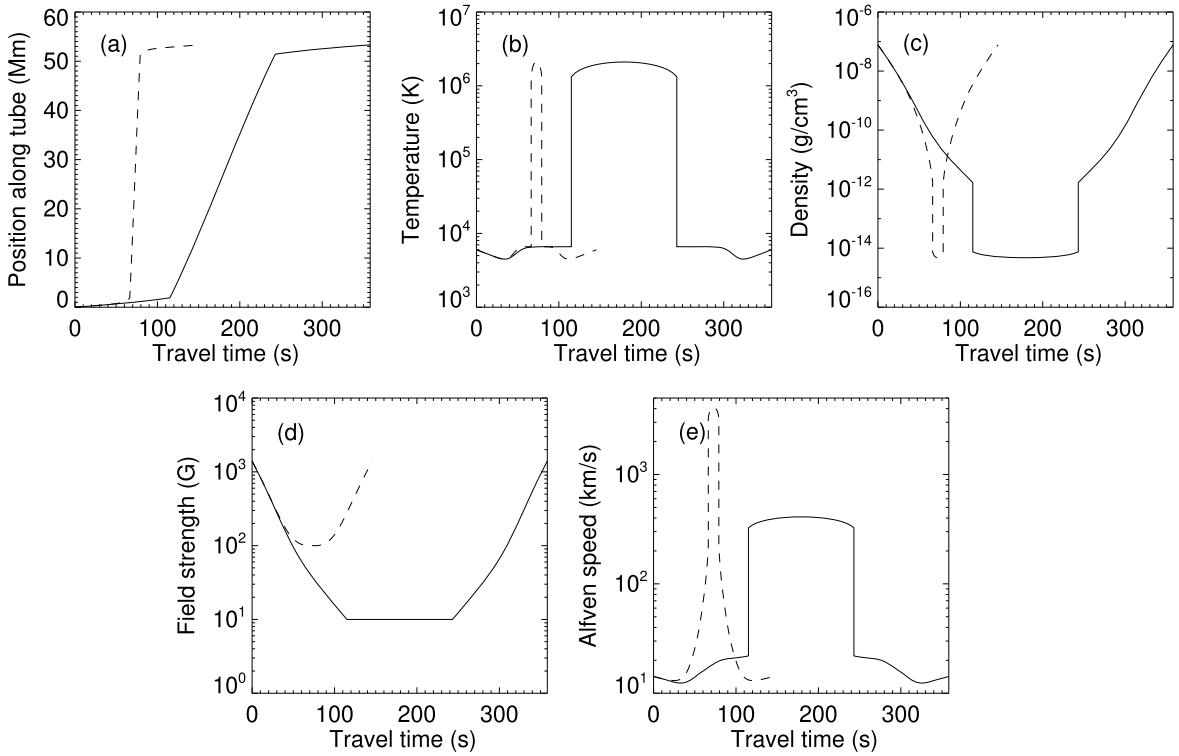

Figure 1. Plasma and magnetic parameters in the initial atmospheres. The panels show temperature (b), density (c), magnetic field strength (d), and Alfvén speed (e) for both the QS model (solid lines) and the AR model (dashed lines lines). All the quantities are shown as a function of Alfvén travel time, corresponding to the distance along the loop (a).

nonlinear effects, $\tau_{\rm nl}$) we set up a number of models with different parameters, altering the coronal magnetic field strength and amplitude of the driver (i.e., ω_0). The atmosphere setup is similar for all simulations. The loop length is about 50 Mm and the radius of the flux tube at the photosphere is $R_{\rm phot} = 100$ km, and the magnetic expansion factor in the corona is $\Gamma = 1$. We note that the loop length in the simulations is shorter than the average loop length reported in previous wave studies (although the observational case studies are biased toward larger loops—see footnote 5). This is for computational efficiency. Increasing the loop length but maintaining the same values for magnetic field strength would lead to longer Alfvén travel times, whereas the nonlinear transfer time remains unchanged as this depends upon the wave amplitude and perpendicular wavenumber. Hence, for loop systems with Alfvén travel times longer than the nonlinear timescale, increasing loop length should have little effect on the final result.

The height of the transition region is fixed at $z_{\rm TR} = 1900$ km, which corresponds to the coronal pressure, $p_{\rm cor} = 1.35\,{\rm dyn\,cm^{-2}}$. Using the scaling law of R. Rosner et al. (1978), the peak temperature then reaches $T_{\rm Max} = 2.3$ MK. Furthermore, gravity is neglected in the corona and the gas pressure is constant along the coronal part of the loop. The plasma parameters and magnetic fields for models of active region and quiet Sun are shown in Figure 1.

The first set of models have a coronal magnetic field strength of $B_{\rm cor} = 100$ G. This value of coronal magnetic field strength is comparable to that estimated in active regions. Hence, we label these models with prefix AR. The average Alfvén speed in the model reaches $v_{\rm A} \sim 3856\,{\rm km\,s^{-1}}$ in the corona (see Figure 1(e)). Hence, these models have a wave travel time in the coronal segment of ∼12 s.

For the AR runs, the simulations are driven with a range of driver amplitudes, where the vorticity at the base is between $\omega_0 = 10^{-3}$ and $3 \times 10^{-2}\,{\rm s^{-1}}$ (see Table 1). The relationship between the vorticity and the rms velocity for the driver modes is $v_{\rm rms} = \sqrt{2} R_{\rm phot}\omega_0/3.382$ (A. A. van Ballegooijen et al. 2011). Hence, the photospheric value of $v_{\rm rms} = 0.04-1.25\,{\rm km\,s^{-1}}$. As the amplitude of the wave driver increases, this effectively decreases the nonlinear timescale (see Equation (3)). A crude approximation for the nonlinear timescale is given in Table 1, and is estimated using the velocity amplitudes in the corona[7] and the radius of the flux tube at the corona to represent the perpendicular scale. Hence, the range of vorticities chosen for the driver enables a sequence of models where the nonlinearity parameter becomes increasingly smaller.

We note that correct values for the photospheric velocities at the base of the active-region loops are ambiguous. In general, estimated photospheric horizontal motions in active regions are $\sim 0.3\,{\rm km\,s^{-1}}$, e.g., moat flows (S. Vargas Domínguez et al. 2008), horizontal flow fields (M. Verma et al. 2016), and flows in plage (A. M. Title et al. 1992). Hence, the wave driver for the AR2 run can be considered as being most representative of typical photospheric horizontal velocities in active regions. Further, in the AR2 run the value of $\zeta \lesssim 1$ is comparable to the ratio of timescales estimated from observations (Section 2) despite the short Alfvén travel time. The runs AR1, AR3, and AR4 are primarily there for didactic purposes.

[7] The velocity amplitude at any point along the loop is calculated as $v_{\rm rms}(z,\,t) = \sqrt{\sum_{k=1}^{N} a_k^2 f_k^2(z,\,t)}\,/R$. Hence the nonlinear timescale calculated using $v_{\rm rms}$ includes all perpendicular scales and underestimates the nonlinear timescale.

Table 1
Wave Parameters and Timescales in the Simulations

Run	Photosphere		Corona				
	ω_0 (s^{-1})	v_{rms} ($km\ s^{-1}$)	v_{rms} ($km\ s^{-1}$)	v_A ($km\ s^{-1}$)	τ_A (s)	τ_{nl} (s)	τ_L (s)
AR1	0.001	0.04	4	3856	12	94	101
AR2	0.01	0.42	30	3856	12	13	101
AR3	0.02	0.84	46	3856	12	8	101
AR4	0.03	1.25	56	3856	12	7	101
QS	0.04	1.48	43	385	120	26	1017

Note. τ_A here is taken as the Alfvén travel time along the coronal segment of the loop.

For the last of set of simulations, we decrease the coronal magnetic field strength to $B_{cor} = 10$ G, one order of magnitude smaller than that of the other simulations.[8] We make this choice in order to obtain a smaller coronal Alfvén speed and consequently a long Alfvén travel time. The average Alfvén speed in the model reaches $v_A \sim 385\ km\ s^{-1}$, which is again in line with estimated wave propagation speeds in the quiet Sun (R. J. Morton et al. 2016; Z. Yang et al. 2020). This model is prefixed with the label QS. Compared to the AR models, the wave timescale for the QS model is a factor of 10 longer, $\tau_A \approx 120$ s.

As discussed in Section 1.1, the amplitudes of the resolved coronal Alfvénic kink waves appear larger in the quiet-Sun loops (15–20 $km\ s^{-1}$) than in active regions (1–4 $km\ s^{-1}$). Hence, the QS run is driven with a vorticity at the base of $\omega_0 = 4 \times 10^{-2}$ ($v_{rms} = 1.48\ km\ s^{-1}$). This value is the same as is used by A. A. van Ballegooijen et al. (2011) for their simulations and is comparable to observed motions of photospheric magnetic bright points (e.g., L. P. Chitta et al. 2012). The increase in driver amplitude, compared to the values used in the AR simulations, leads to larger values of the coronal wave amplitude in the QS run.

4. Results and Discussion

The overall behavior of the simulations is similar to that discussed extensively by A. A. van Ballegooijen et al. (2011). The driver modes generate rotational Alfvén waves, which propagate upward and reflect due to inhomogeneity along the magnetic field line (i.e., variation in Alfvén speed). For nonlinear waves, this reflection leads to interaction of the counterpropagating waves that enables the onset of the turbulent cascade.

The simulated times are 3000 s, which is enough time for the simulations to reach a turbulent state. In the AR models, the run time is equivalent to $\sim 230\, t_A$, which should enable many interactions of counterpropagating wave packets. A more precise estimate for the nonlinearity parameter (than that used in the previous section) is calculated for the simulations as

$$\zeta_j \equiv \frac{k_{\perp,j} v_{\perp,j}}{\tilde{\omega}_j}, \tag{24}$$

where the subscript j refers to bin number. For each j, wave modes are summed over for the perpendicular wavenumbers, a_k, which lie in the bin range $j\Delta a < a_k < (j+1)\Delta a$ ($j = 0, \ldots, 12$). Here $\Delta a = 2$ is the bin size in wavenumber space. Full details on how the average perpendicular velocity, $v_{\perp,j}$ and the average frequency $\tilde{\omega}_j$ are calculated are given by A. A. van Ballegooijen et al. (2011). Another timescale of some interest is the leakage time, which measures the loss of wave energy from the coronal segment of the loop to the lower solar atmosphere (as the transition region is a semipermeable barrier). This can be estimated using the following formula from linear theory (D. Berghmans & P. de Bruyne 1995; L. Ofman 2002). Assuming the coronal segment of the loop behaves as a resonant cavity with imperfectly line-tied boundaries, the leakage time is given by

$$\tau_L = \frac{L_C}{|\ln R| v_{AC}}. \tag{25}$$

Here τ_L is the leakage time, L_C is the coronal loop length, R is the reflection coefficient at the transition region part of the loop, and v_{AC} is the average Alfvén speed in the corona ($v_{AC} \sim 385\ km\ s^{-1}$ in the quiet Sun and $\sim 3856\ km\ s^{-1}$ in an active region). In our model the reflection coefficient is around 0.87 and is given by $R = (c-1)/(c+1)$ (see A. A. van Ballegooijen et al. 2011) where c is the ratio of the Alfvén speeds below and above the discontinuity point. We estimate the leakage timescale as ~951 s for quiet-Sun simulation and ~95 s for active-region models.

Hence, this is much longer than the Alfvén travel time and the nonlinear timescale in both simulations (see Table 1), although leakage of wave energy there will still influence the energy buildup and dissipation in the corona, as demonstrated by A. Verdini et al. (2012).

4.1. Comparison of Models

First we discuss results of the AR simulations. For AR1, the simulation is dominated by linear wave dynamics. The linear nature of the system is demonstrated by the small value for the wavenumber-binned nonlinearity parameter (Figures 2(d), (e), and (f)). The maximum fluctuations in the coronal part of the loop are $v_{rms} = 4\ km\ s^{-1}$ (Table 1). To reveal aspects of the dynamics within the system we can examine how the perturbations behave in the coronal segment of the loop. For this, we use the evolution of the parallel vorticity $\omega(z, t)$ (see Equation (19)), which is averaged over the cross section of the tube and wavenumber. In Figure 2(a) we show the power spectra of $\omega(z, t)$ obtained by taking the Fourier transform of the time series at each spatial location, $\Omega(z, f)$. The results show a clear structure in the power spectrum. A number of bright horizontal bands are seen at regular intervals in frequency, corresponding to the resonant modes of the coronal segment of the loop. Multiple harmonics of the system are visible, up to around $n = 9$ for the frequency range shown. The plot shows the horizontal bands have greater power at selected spatial locations in the coronal cavity, and lower power at other locations. These correspond to the antinodes and nodes, respectively, of standing-mode oscillations (a similar pattern is shown for standing kink modes by A. N. Afanasyev et al. 2020). It is straightforward to confirm that the location of the enhanced power in frequency–distance space is broadly in line with the expected resonant frequencies from Equation (1), which, for $v_{AC} = 3856\ km\ s^{-1}$ and $L_C = 49{,}500$ km, gives $f_n = \{0.039, 0.078, 0.117, 0.156, 0.195, \ldots\}$ Hz for the first

[8] We discuss our choice of magnetic and plasma conditions in this model in the Appendix.

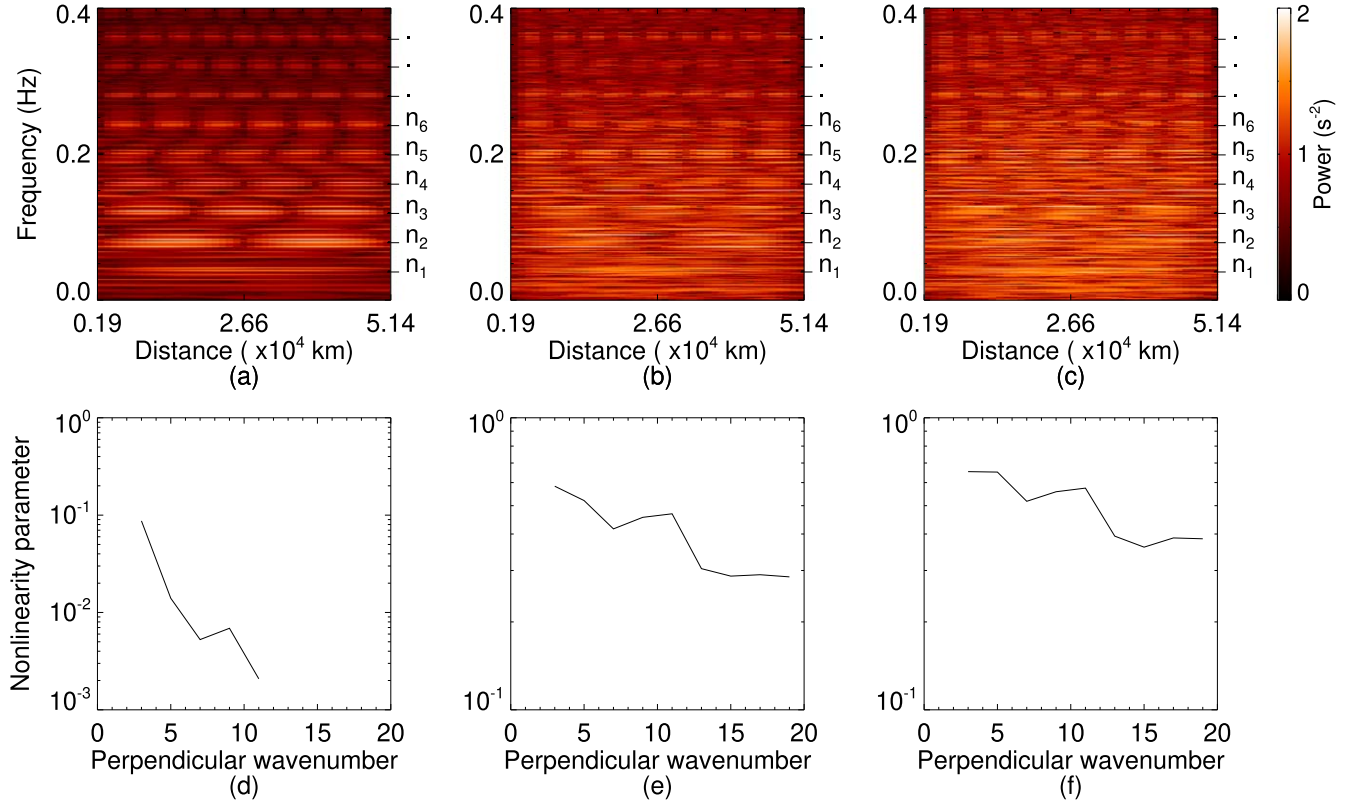

Figure 2. Results for the additional active-region simulations: AR1 ($\omega_0 = 0.001$ s^{-1}, left column), AR3 ($\omega_0 = 0.02$ s^{-1}, middle), and AR4 ($\omega_0 = 0.03$ s^{-1}, right). The top row displays the vorticity power spectrum, $\Omega(z, f)$, as a function of frequency for each pixel in the coronal segment of the loop. Estimated frequencies for resonant modes in the coronal cavity are indicated on the right-hand axis, specified by the harmonic number (e.g., n_1 is the fundamental mode). The first six are noted and three subsequent ones are indicated without label. The bottom row is the associated nonlinearity parameter ($\zeta = k_\perp v_\perp / \tilde{\omega}$) as a function of dimensionless perpendicular wavenumber ($a_\perp$) in the corona for each simulation.

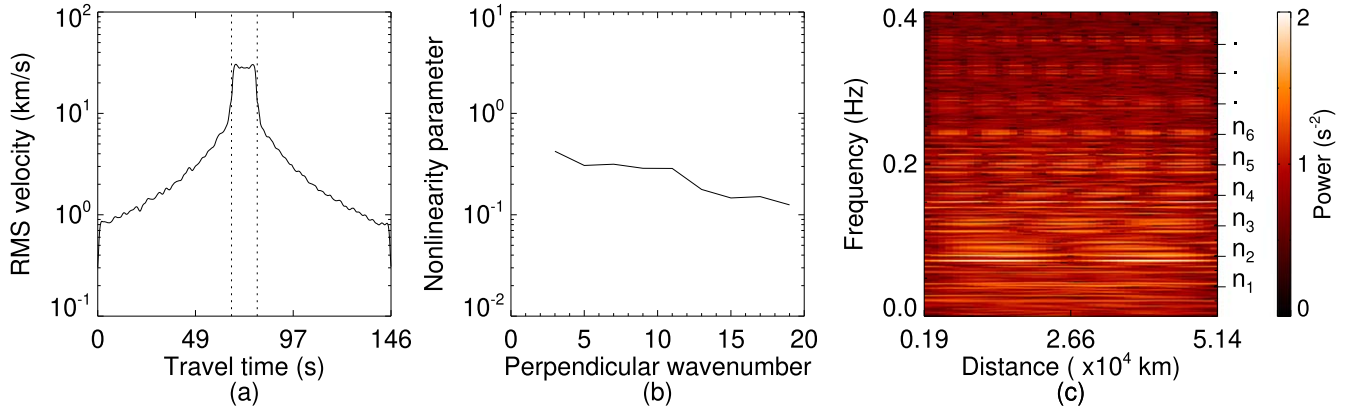

Figure 3. Results for the AR2 simulation run. (a) The rms velocity plotted as a function of position along the loop. The position has been given in terms of Alfvén travel time. The vertical dotted lines indicate the transition region. (b) The nonlinearity parameter ($\zeta = k_\perp v_\perp / \tilde{\omega}$) vs. dimensionless perpendicular wavenumber ($a_\perp$) in the coronal part of the loop. (c) The power spectra of parallel vorticity, $\Omega(z, f)$, shown as a function of frequency for each pixel in the coronal segment of the loop. Multiple harmonics are visible due to the resonance of the system.

five harmonics (the frequencies up to $n = 9$ are indicated on the plot).

Figure 3 shows the results for the simulation of AR2. We remind the reader that this simulation is the one with footpoint driving amplitudes closest to measured horizontal photospheric flow speeds in active regions (i.e., 0.3 km s^{-1}; M. Verma et al. 2016). The maximum amplitude of the fluctuations in the coronal part of the loop is $\delta v = 30.5$ km s^{-1} (Figure 3(a)). This velocity amplitude is larger than amplitudes reported for the decayless kink oscillations in active-region loops (e.g., S. A. Anfinogentov et al. 2015); however, here $v_{\rm rms}$ is integrated over many modes of oscillation, while the observations correspond to measurements of one mode.

In the AR2 simulation, the coronal nonlinearity parameter is larger than in AR1 (Figure 3(b)). As Figure 3(b) shows, the nonlinearity parameter is below 0.4, confirming that the linear wave dynamics in the system are still dominant over the nonlinear dynamics. Figure 3(c) shows the coronal power spectrum where the presence of resonant modes is still visible, although not as distinguished as in the AR1 run (Figure 2(a)). The presence of resonant modes in a weak turbulence regime is in line with the results of G. Nigro et al. (2008, coronal-only

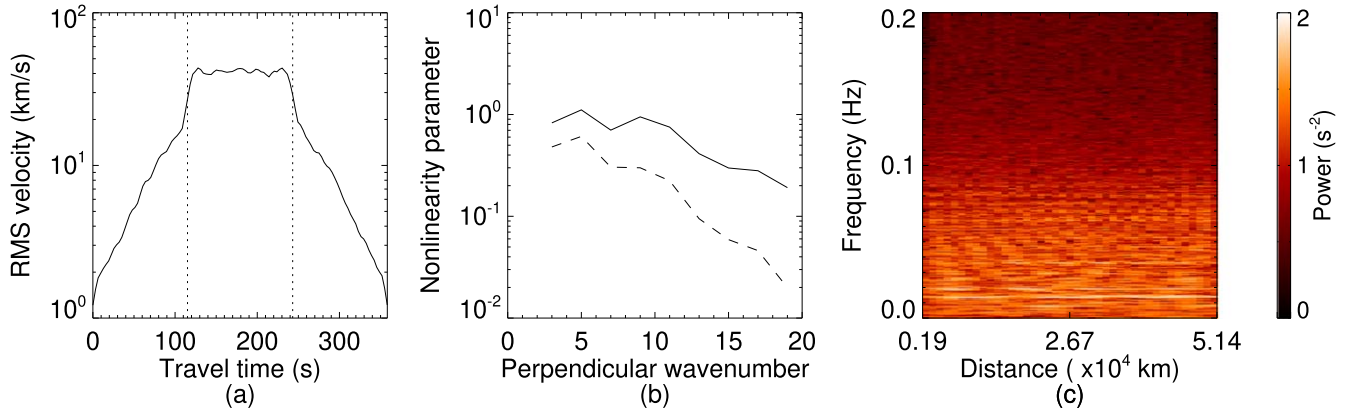

Figure 4. Results for the QS simulation run. The panels are the same as in Figure 3. In panel (b) we also show the nonlinearity parameter vs. dimensionless perpendicular wavenumber in the chromosphere (dashed line). In panel (c), no evidence of resonances is present in the coronal cavity.

model) and A. Verdini et al. (2012, three-layer atmosphere model).

Figure 4 displays the results for the QS run. The larger amplitude of the footpoint driver (compared to the AR runs) gives a maximum fluctuation amplitude in the coronal part of the loop of $\sim$43 km s^{-1} (Figure 4(a)). Again, this is larger than the measured values for propagating waves, but it is an integration of many modes. Figure 4(b) shows the corresponding nonlinearity parameter. which is of the order of unity up until at least a perpendicular wavenumber $j = 10$. At the larger wavenumbers, the damping employed in the simulations acts to cause ζ_j to become smaller than one (A. A. van Ballegooijen et al. 2011). The large nonlinearity parameters indicate that in this run the system is in a strong turbulence regime, with nonlinear dynamics dominating over the linear wave dynamics.

Figure 4(c) shows the corresponding power spectra for the QS run. In contrast to AR1 and AR2, we see no clear pattern of standing-wave formation in this system. As mentioned in Section 2, we suggest that this is because the dominant nonlinear dynamics suppresses the formation of resonances in the system. With the nonlinear time less than or comparable to the Alfvén travel time, the wave packets are distorted significantly as they propagate along the loop.

Another measure of the level of nonlinearity of the waves that is often used is the ratio of wave amplitude to Alfvén speed ($v_{\rm rms}/v_{\rm A}$), which is shown in Figure 5. This measure is proportional to ζ (Equation (4)), but does not account for anisotropy between the parallel and perpendicular directions (i.e., $k_\perp/k_\parallel$). It is clear that in the AR2 run the ratio of wave amplitude to Alfvén speed is an order of magnitude smaller everywhere than it is in the QS run. Hence, the waves in the AR2 run have a lower degree of nonlinearity throughout the entire atmosphere than those in the QS run.

The results from AR3 and AR4 confirm that resonances are suppressed because the nonlinear timescale is comparable to the wave timescale. In these runs, the amplitude of the driver wave is increased by factors of 2 and 3 from the AR2 run, respectively. The increase in amplitude leads to an increase in the degree of nonlinearity of the waves and decreases the nonlinear timescale. This is reflected in the increasing nonlinearity parameter in the corona (see Figures 2(e) and (f) and Figure 5), although the values are not as large as those of the QS run. Figures 2(b) and (c) show the power spectra from the AR3 and AR4 runs. When comparing these to the power spectrum from AR1, the presence of the standing modes is seen

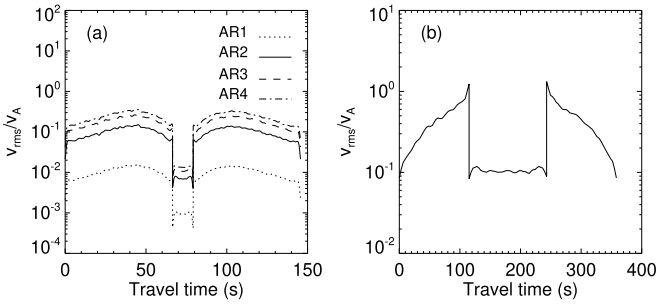

Figure 5. The ratio of wave amplitude to Alfvén speed along the loop for the AR2 run (a) and the QS run (b). Positions are given in terms of Alfvén travel time.

to fade through panels Figures 2(a), (b), and (c), indicating that a smaller fraction of the total energy is contained within the resonant modes as the strength of turbulence is increased. It can also be seen that the lower-frequency resonant modes (e.g., fundamental, first overtone) are subject to greater energy loss through turbulence. This is due to larger wave amplitudes at the lower frequencies, hence greater nonlinearity (as seen in Figures 2(e) and (f)).

So far we have discussed the strength of the turbulence only in reference to the nonlinearity parameter. However, we can also gain insights from estimating the efficiency of dissipation, which was defined by P. Dmitruk & W. H. Matthaeus (2003) as the energy dissipation within a region divided by the energy flux. As derived by A. A. van Ballegooijen et al. (2011), the dissipation rate averaged over the cross section is given by

$$Q(z,t) = Q_{\rm kin} + Q_{\rm mag} = \frac{\rho_0}{R^2}\sum_{k=1}^{N}\nu_k a_k^2 f_k^2 + \frac{B_0^2}{4\pi R^2}\sum_{k=1}^{N}\nu_k a_k^2 h_k^2, \quad (26)$$

where ν_k is the damping rate. We then define the energy flux as

$$F_{\rm A} = \rho v_{\rm rms}^2 v_{\rm A}, \quad (27)$$

where $v_{\rm rms}$ is the amplitude of the footpoint driver, and ρ and $v_{\rm A}$ are taken as the density and Alfvén speed at the footpoint of the loop. Hence, the efficiency of dissipation is estimated as

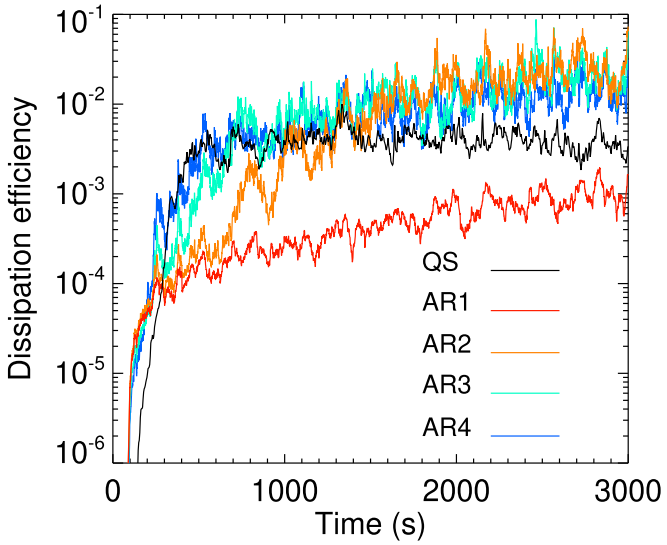

Figure 6. Dissipation efficiency for each simulation.

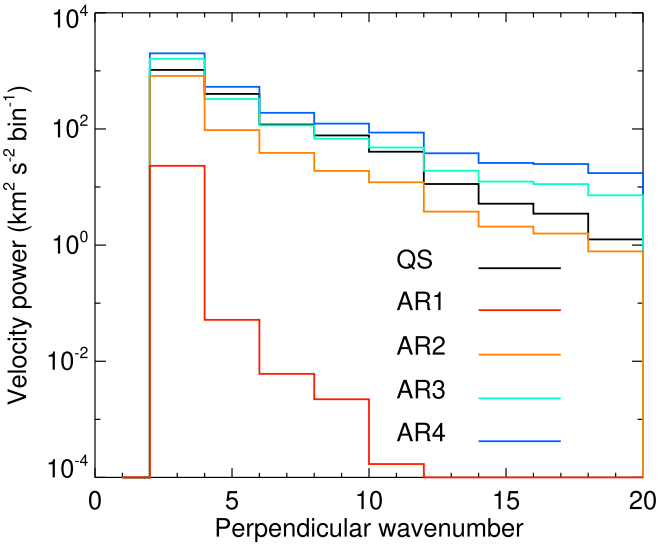

Figure 7. The power spectrum of coronal velocity as a function of perpendicular wavenumber ($a_\perp$) for all simulations.

(P. Dmitruk & W. H. Matthaeus 2003)

$$\epsilon = \frac{\int Q(z, t) dz}{F_A}, \tag{28}$$

with the integration over the relevant region of the loop.

Figure 6 shows the dissipation efficiency integrated over the coronal volume from all the simulations. It reveals how quickly turbulence develops within the coronal cavity. For AR1 we see that the dissipation efficiency is low compared to the other models. This should be expected as this simulation is strongly dominated by the linear wave dynamics, so the development of nonlinear phenomena happens slowly. However, the dissipation efficiency continues to increase, suggesting that the system might reach a fully turbulent state. The two runs with short nonlinear timescales, QS and AR4 (see Table 1), show a much more rapid development of the turbulence within the system, with dissipation efficiency reaching a steady state. It is seen from the curves in Figure 6 that QS reaches this steady state sooner than AR4. Simulations for AR2 and AR3 also reach comparable levels of dissipation efficiency to the QS and AR4 runs. So across all systems, turbulence is developed or developing. The presence of turbulence in most runs can also be inferred from the power spectrum of coronal velocity for perpendicular wavenumbers. Figure 7 demonstrates that there is power across a broad range of perpendicular wavenumbers for all simulations, except AR1, which has low levels of nonlinearity and hence the cascade is inefficient.

The curves for turbulence efficiency support our suggestion about the ordering of the timescales associated with wave dynamics and nonlinearity. When the timescales for nonlinear dynamics are long compared to the Alfvén travel time, resonant (standing) modes can form in the coronal cavity. This happens because there is sufficient time before the turbulence is developed enough to substantially dissipate the wave energy within the resonances. Conversely, when the nonlinear dynamics are of the order of (or shorter than) the Alfvén travel time, this leads to a rapid development of a fully turbulent system. The strength of the nonlinear interactions can significantly distort the propagating wave packets, causing decorrelation on lengths scales $l_\parallel \sim v_A \tau_{nl}$. Hence, if the nonlinear timescale is substantially shorter than the Alfvén travel time the effective parallel length scale is shorter than the loop length. This prevents the formation of resonant modes.

4.2. Rotational versus Kink

It is worth considering how these results apply to the observed Alfvénic waves, i.e., the kink mode. While on the surface this may appear a significant difference, we believe that our results are also relevant to kink modes. The fundamental radial ($m \neq 0$) non-axisymmetric modes of a magnetic cylinder have been shown to be Alfvénic in nature, and can also be adequately described as surface Alfvén modes (M. Goossens et al. 2009, 2012). The surface Alfvén modes will be subject to similar nonlinear interactions and cascades to shear Alfvén modes but with additional effects that could influence the development of turbulence, such as self-interaction (N. Magyar et al. 2017, 2019; R. Ismayilli et al. 2022; T. Van Doorsselaere et al. 2024), resonant absorption (e.g., J. A. Ionson 1978; J. V. Hollweg & G. Yang 1988), and instabilities (P. Antolin et al. 2014). The relative magnitude of the additional physics for surface Alfvén modes is highly dependent on the magnitude of density inhomogeneity perpendicular to the magnetic field (R. J. Morton et al. 2023). Observations indicate that the density inhomogeneity is large in active regions and marginal in the quiet-Sun coronal loops (R. J. Morton et al. 2021). Hence, these other effects would be weak in the quiet-Sun coronal loops and could have little effect on the development of turbulence.

While there are subtle differences between the physical properties of the kink and rotational Alfvén modes, the literature is littered with results that show only minor differences in the actual behavior of the two modes. For example, both modes are also subject to the same variations in eigenmode oscillations under density stratification along the flux tube. R. J. Morton et al. (2011) have noted that governing equations for torsional modes and kink modes in a coronal loop are of the same form, with the eigenvalues differing only by a multiplicative constant; see also M. V. Dymova & M. S. Ruderman (2006) for kink modes and R. J. Morton et al. (2011) for torsional Alfvén modes.

Both modes also are subject to atmospheric cutoffs (and reflections) that depend on the gradients of Alfvén speed; see,

e.g., R. Hammer et al. (2010) for torsional modes and S. Routh et al. (2013) and I. Lopin & I. Nagorny (2017) for kink modes (and also K. Murawski & Z. E. Musielak 2010 for shear Alfvén waves). The modes even have similar responses in multifluid plasma, e.g., to damping by ambipolar diffusion (R. Soler et al. 2009).

The subtle differences could lead to important consequences for the way turbulence develops for the nonrotational Alfvénic waves. It was demonstrated by M. Goossens et al. (2012) that only the fundamental radial modes for non-axisymmetric $m \neq 0$ oscillations are surface Alfvénic modes. The higher-order radial modes are more like fast MHD waves (i.e., they possess a significant compressibility), hence when $k_z R \lesssim 1$ the modes are not trapped and wave energy leaks from the flux tube via MHD radiation. The process of the cascade of wave energy introduced in the simulations occurs in both the azimuthal and radial wavenumbers. This could indicate, for nonrotational Alfvénic modes, that wave energy will only remain trapped in the loop when cascading via the azimuthal wavenumber and will be radiated away for cascades in radial wavenumber, although the degree of wave energy lost may well depend on the relative sizes of the nonlinear interaction time and the leakage time associated with MHD radiation. This aspect would seemingly not influence our main hypothesis, that standing modes are not formed if turbulence is strong.

5. Conclusion

Motivated by observations of coronal Alfvénic waves, we examined whether the development of turbulence could suppress the formation of standing-mode oscillations in a coronal loop with continuous photospheric footpoint motions. Our numerical study focused on the cascade of torsional Alfvén modes but we suggest the results would be applicable to other Alfvénic modes in an inhomogeneous plasma. Using a semi-realistic atmosphere as a background for the waves to propagate in, we find that standing modes are suppressed when the loop system has nonlinear timescales shorter than wave timescales. We suggest this is because there is not sufficient time for the waves to travel the required distance (i.e., two loop lengths) before nonlinear interactions significantly decorrelate the wave packets, cascading the wave energy to higher-order radial and azimuthal modes.

Approximate estimates of wave and nonlinear timescales in the quiet Sun and active regions, based upon observations, suggest that $\tau_A \gtrsim \tau_{nl}$ in the quiet Sun, while $\tau_A \lesssim \tau_{nl}$ in active regions. Hence, the results from the simulations presented offer a potential reason as to why (apparently) only propagating modes are observed in the quiet Sun, whereas some active-region loops support standing modes.

We reiterate that both quiet-Sun and active-region loops can still support wave turbulence. The difference is that the turbulence in the quiet Sun is able to develop faster than the linear wave timescales for resonant modes, while the time to develop a turbulent system in the active regions is longer than the linear wave timescales.

Acknowledgments

E.T. and R.J.M. would like to thank the UKRI for financial support via a UKRI Future Leader Fellowship (RiPSAW MR/T019891/1). We would like to thank F. Malara, H. Miriyala, T. Duckenfield, R. Sharma, and N. Balodhi for reading drafts and valuable discussions.

Data Availability

The data underlying this article are available on Zenodo: doi:10.5281/zenodo.14833984.

Appendix
Comments on Parameters of the Simulations

We use this appendix to provide some comments on plasma and magnetic parameters used in the different simulation runs.

A.1. Loop Length

As commented in the main text, the loop length used in the simulations corresponds to a short coronal loop. If the loop length were increased then this would lead to longer Alfvén travel times. For the QS simulation run this would make no difference because the nonlinear timescale is already shorter than the Alfvén travel time. Hence the suppression of resonances would still occur and is expected in longer loops.

A.2. QS Plasma and Magnetic Field Values

We acknowledge that the QS model does not represent certain estimated aspects of the coronal plasma in the quiet Sun. The value of $B_{cor} = 10$ G is larger than estimates of the quiet-Sun magnetic field obtained from coronal seismology (Z. Yang et al. 2020), and the coronal plasma density in the model is also an order of magnitude more than estimated from observations (e.g., G. Del Zanna et al. 2019). The use of these values arises in part from a practical standpoint but we believe it does not change the results substantially.

From a practical perspective, using values $B_{cor} < 10$ G leads to violations of the thin-tube approximation in the upper chromosphere with the current atmospheric profile, with the magnetic scale height becoming much smaller than the tube radius. We would prefer to avoid such situations because they violate the assumptions used to derive the RMHD equations.

Importantly, what is key to the experiments in this work is the ordering of the timescales of the wave dynamics and nonlinear timescales that define the development of turbulence (e.g., P. Dmitruk & W. H. Matthaeus 2003; A. A. Schekochihin 2022). As long as this ordering is preserved, it is expected that the overall evolution of the turbulence in the corona will remain broadly similar to what is discussed.

The combination of ρ_{cor} and B_{cor} values used in the QS simulation leads to an Alfvén speed in the loop comparable to that estimated in the quiet-Sun loops. Hence, if we rescale the values in line with observationally derived estimates, say $B_{cor} = 3$ G and $\rho_{cor} = 10^{-15}$ g cm^{-3}, then the Alfvén speed in the corona is largely unchanged. Hence the nonlinear time will still be shorter than the Alfvén travel time. Furthermore, we expect no difference in the wave dynamics in the corona. The transmission and reflection of Alfvén waves into and out of the corona is also largely unchanged as the coefficients depend on the ratio of Alfvén speeds (see Equation (B25) of A. A. van Ballegooijen et al. 2011).

We note that, in general, it is known that changing the magnetic field strength and density will impact the evolution of the turbulence. In the RMHD regime, the turbulence is only unchanged if the rest of the system is rescaled simultaneously

(A. Beresnyak 2011). Varying only B_{cor} and ρ_{cor} in the current system subsequently leads to changes in the two timescales (unless changes in B are proportional to $\rho^{1/2}$). For example, decreasing B_{cor} influences the gradient of Alfvén speed across the transition region, which affects the wave amplitudes in the corona and hence τ_{nl} (e.g., A. A. van Ballegooijen et al. 2011).

Finally, due to the small magnetic field strength in the quiet Sun, gravity and loop expansion could potentially become more important in wave dynamics (e.g., A. A. van Ballegooijen et al. 2011). It was suggested by A. A. van Ballegooijen et al. (2011) that loop expansion leads to increased wave energy flux in the corona due to increased Alfvén travel times. Such a phenomenon would only act to increase ζ. However, assuming the quiet-Sun loops are in hydrostatic equilibrium, then, by considering pressure balance, the density should vary in proportion to B^2. Hence, there is no expected change in the Alfvén speed along the coronal part of a loop in hydrostatic equilibrium. Thus we expect the inclusion of gravity and loop expansion to have little influence in an incompressible model of Alfvén waves.

ORCID iDs

Edris Tajfirouze https://orcid.org/0000-0003-3754-7045
Richard Morton https://orcid.org/0000-0001-5678-9002
Mahboubeh Asgari-Targhi https://orcid.org/0000-0003-0204-8385

References

Afanasyev, A. N., Van Doorsselaere, T., & Nakariakov, V. M. 2020, A&A, 633, L8
Anfinogentov, S. A., & Nakariakov, V. M. 2019, ApJL, 884, L40
Anfinogentov, S. A., Nakariakov, V. M., & Nisticò, G. 2015, A&A, 583, A136
Antolin, P., & Rouppe van der Voort, L. 2012, ApJ, 745, 152
Antolin, P., Yokoyama, T., & Van Doorsselaere, T. 2014, ApJL, 787, L22
Arregui, I. 2015, RSPTA, 373, 20140261
Aschwanden, M. J., Fletcher, L., Schrijver, C. J., & Alexander, D. 1999, ApJ, 520, 880
Aschwanden, M. J., Nightingale, R. W., & Alexander, D. 2000, ApJ, 541, 1059
Asgari-Targhi, M., Brooks, D. H., Hahn, M., et al. 2024, ApJ, 968, 7
Asgari-Targhi, M., van Ballegooijen, A. A., & Imada, S. 2014, ApJ, 786, 28
Beresnyak, A. 2011, PhRvL, 106, 075001
Beresnyak, A. 2015, ApJL, 801, L9
Berghmans, D., & de Bruyne, P. 1995, ApJ, 453, 495
Boldyrev, S. 2005, ApJL, 626, L37
Brooks, D. H., & Warren, H. P. 2016, ApJ, 820, 63
Brooks, D. H., Warren, H. P., Ugarte-Urra, I., & Winebarger, A. R. 2013, ApJL, 772, L19
Chitta, L. P., van Ballegooijen, A. A., Rouppe van der Voort, L., DeLuca, E. E., & Kariyappa, R. 2012, ApJ, 752, 48
De Pontieu, B., Carlsson, M., Rouppe van der Voort, L. H. M., et al. 2012, ApJL, 752, L12
Del Zanna, G., Gupta, G. R., & Mason, H. E. 2019, A&A, 631, A163
Dmitruk, P., & Matthaeus, W. H. 2003, ApJ, 597, 1097
Duckenfield, T. J., Goddard, C. R., Pascoe, D. J., & Nakariakov, V. M. 2019, A&A, 632, A64
Dymova, M. V., & Ruderman, M. S. 2006, A&A, 459, 241
Elsasser, W. M. 1950, PhRv, 79, 183
Goddard, C. R., Nisticò, G., Nakariakov, V. M., & Zimovets, I. V. 2016, A&A, 585, A137
Goldreich, P., & Sridhar, S. 1995, ApJ, 438, 763
Goossens, M., Andries, J., Soler, R., et al. 2012, ApJ, 753, 111
Goossens, M., Erdélyi, R., & Ruderman, M. S. 2011, SSRv, 158, 289
Goossens, M., Terradas, J., Andries, J., Arregui, I., & Ballester, J. L. 2009, A&A, 503, 213
Hammer, R., Musielak, Z. E., & Routh, S. 2010, AN, 331, 593
Hollweg, J. V. 1981, SoPh, 70, 25
Hollweg, J. V. 1983, in Solar Wind Five, NASA Conf. Publication, 2280 (Washington, DC: NASA), 5
Hollweg, J. V. 1984, ApJ, 277, 392
Hollweg, J. V., & Yang, G. 1988, JGR, 93, 5423
Ionson, J. A. 1978, ApJ, 226, 650
Ionson, J. A. 1982, ApJ, 254, 318
Ismayilli, R., Van Doorsselaere, T., Goossens, M., & Magyar, N. 2022, FrASS, 8, 241
Karampelas, K., & Van Doorsselaere, T. 2020, ApJL, 897, L35
Kohutova, P., Verwichte, E., & Froment, C. 2020, A&A, 633, L6
Lopin, I., & Nagorny, I. 2017, AJ, 154, 141
Magyar, N., Van Doorsselaere, T., & Goossens, M. 2017, NatSR, 7, 14820
Magyar, N., Van Doorsselaere, T., & Goossens, M. 2019, ApJ, 882, 50
Malanushenko, A., Cheung, M. C. M., DeForest, C. E., Klimchuk, J. A., & Rempel, M. 2022, ApJ, 927, 1
Mandal, S., Tian, H., & Peter, H. 2021, A&A, 652, L3
McIntosh, S. W., de Pontieu, B., Carlsson, M., et al. 2011, Natur, 475, 477
Meyrand, R., Galtier, S., & Kiyani, K. H. 2016, PhRvL, 116, 105002
Meyrand, R., Kanekar, A., Dorland, W., & Schekochihin, A. A. 2019, PNAS, 116, 1185
Morton, R. J., & Cunningham, R. 2023, ApJ, 954, 90
Morton, R. J., Ruderman, M. S., & Erdélyi, R. 2011, A&A, 534, A27
Morton, R. J., Sharma, R., Tajfirouze, E., & Miriyala, H. 2023, RvMPP, 7, 17
Morton, R. J., Tiwari, A. K., Van Doorsselaere, T., & McLaughlin, J. A. 2021, ApJ, 923, 225
Morton, R. J., Tomczyk, S., & Pinto, R. 2015, NatCo, 6, 7813
Morton, R. J., Tomczyk, S., & Pinto, R. F. 2016, ApJ, 828, 89
Morton, R. J., Weberg, M. J., & McLaughlin, J. A. 2019, NatAs, 3, 223
Murawski, K., & Musielak, Z. E. 2010, A&A, 518, A37
Nakariakov, V. M., Anfinogentov, S. A., Nisticò, G., & Lee, D. H. 2016, A&A, 591, L5
Nakariakov, V. M., & Kolotkov, D. Y. 2020, ARA&A, 58, 441
Nakariakov, V. M., Kolotkov, D. Y., & Zhong, S. 2022, MNRAS, 516, 5227
Nakariakov, V. M., Ofman, L., Deluca, E. E., Roberts, B., & Davila, J. M. 1999, Sci, 285, 862
Nazarenko, S. V., & Schekochihin, A. A. 2011, JFM, 677, 134
Nechaeva, A., Zimovets, I. V., Nakariakov, V. M., & Goddard, C. R. 2019, ApJS, 241, 31
Nigro, G., Malara, F., & Veltri, P. 2008, ApJ, 685, 606
Nisticò, G., Nakariakov, V. M., & Verwichte, E. 2013, A&A, 552, A57
Ofman, L. 2002, ApJL, 568, L135
Oughton, S., & Matthaeus, W. H. 2020, ApJ, 897, 37
Petrova, E., Magyar, N., Van Doorsselaere, T., & Berghmans, D. 2023, ApJ, 946, 36
Rappazzo, F., Velli, M., Einaudi, G., & Dahlburg, R. 2007, AGUSM, 2007, SH23C–07
Reale, F. 2014, LRSP, 11, 4
Roberts, B. 1981, SoPh, 69, 27
Rosner, R., Tucker, W. H., & Vaiana, G. S. 1978, ApJ, 220, 643
Routh, S., Musielak, Z. E., & Hammer, R. 2013, ApJ, 763, 44
Ruderman, M. S., & Roberts, B. 2002, ApJ, 577, 475
Schekochihin, A. A. 2022, JPlPh, 88, 155880501
Sharma, R., & Morton, R. J. 2023, NatAs, 7, 1301
Soler, R., Oliver, R., & Ballester, J. L. 2009, ApJ, 699, 1553
Strauss, H. R. 1976, PhFl, 19, 134
Strauss, H. R. 1997, JPlPh, 57, 83
Terradas, J., Arregui, I., Oliver, R., et al. 2008, ApJ, 679, 1611
Tian, H., McIntosh, S. W., Wang, T., et al. 2012, ApJ, 759, 144
Title, A. M., Topka, K. P., Tarbell, T. D., et al. 1992, ApJ, 393, 782
Tiwari, A. K., Morton, R. J., & McLaughlin, J. A. 2021, ApJ, 919, 74
Tomczyk, S., McIntosh, S. W., Keil, S. L., et al. 2007, Sci, 317, 1192
van Ballegooijen, A. A., Asgari-Targhi, M., Cranmer, S. R., & DeLuca, E. E. 2011, ApJ, 736, 3
Van Doorsselaere, T., Li, B., Goossens, M., Hnat, B., & Magyar, N. 2020, ApJ, 899, 100
Van Doorsselaere, T., Magyar, N., Sieyra, M. V., & Goossens, M. 2024, JPlPh, 90, 905900113
Van Doorsselaere, T., Nakariakov, V. M., Young, P. R., & Verwichte, E. 2008, A&A, 487, L17
Vargas Domínguez, S., Rouppe van der Voort, L., Bonet, J. A., et al. 2008, ApJ, 679, 900
Verdini, A., Grappin, R., & Velli, M. 2012, A&A, 538, A70
Verma, M., Denker, C., Balthasar, H., et al. 2016, A&A, 596, A3
Verwichte, E., Nakariakov, V. M., Ofman, L., & Deluca, E. E. 2004, SoPh, 223, 77
Wang, T., Ofman, L., Davila, J. M., & Su, Y. 2012, ApJL, 751, L27
Wentzel, D. G. 1979, ApJ, 227, 319
Yang, Z., Bethge, C., Tian, H., et al. 2020, Sci, 369, 694
Zimovets, I. V., & Nakariakov, V. M. 2015, A&A, 577, A4